Correlation between Local Structure Order and Spatial Heterogeneity in a Metallic Glass

Fan Zhu,[1,2] Akihiko Hirata,[2,3] Pan Liu,[1] Shuangxi Song,[1] Yuan Tian,[4] Jiuhui Han,[2] Takeshi Fujita,[2] and Mingwei Chen[1,2,4,*]
[1]State Key Laboratory of Metal Matrix Composites, School of Materials Science and Engineering, Shanghai Jiao Tong University, Shanghai 200030, China
[2]Advanced Institute for Materials Research, Tohoku University, Sendai 980-8577, Japan
[3]Mathematics for Advanced Materials-OIL, AIST-Tohoku University, Sendai 980-8577, Japan
[4]Department of Materials Science and Engineering, Johns Hopkins University, Baltimore, Maryland 21218, USA
(Received 1 June 2017; revised manuscript received 29 August 2017; published 20 November 2017)

Although nanoscale spatial heterogeneity of metallic glasses has been demonstrated by extensive experimental and theoretical investigations, the nature of spatial heterogeneity remains poorly known owing to the absence of a structural depiction of the inhomogeneity from experimental insight. Here we report the experimental characterization of the spatial heterogeneity of a metallic glass by utilizing state-of-the-art angstrom-beam electron diffraction and scanning transmission electron microscopy. The sub-nanoscale electron diffraction reveals that the nanoscale spatial heterogeneity and corresponding density fluctuation have a close correlation with the local structure variation from icosahedronlike to tetragonal crystal-like order. The structural insights of spatial heterogeneity have important implications in understanding the properties and dynamics of metallic glasses.

DOI: 10.1103/PhysRevLett.119.215501

Extensive experiments and computational simulations have demonstrated that the dynamic response of metallic glasses to external excitation is spatially heterogeneous in the nanoregime [1–8], although disordered metallic glasses have been traditionally regarded as homogeneous materials. The spatial heterogeneity has a strong correlation with the mechanical properties [9–11] and dynamics [12–15] of metallic glasses. Several prevailing models, such as free volume [16], shear transformation zones (STZs) [17–20], atomic level stress [21,22], liquidlike zones [7], flow units [8], and flexibility volume [9], have been postulated to describe the heterogeneity. These models are usually based on the assumption of a structural defect or inefficient local atomic packing in metallic glasses which leads to the formation of heterogeneously dense and loose regions. By utilizing amplitude-modulation dynamic atomic force microscopy (AM AFM), the nanoscale heterogeneous response of viscoelasticity has been visualized in real space from different metallic glasses [12,23–26]. However, the nature of the nanoscale domains with different viscoelasticity cannot be disclosed by AM AFM, and, accordingly, the structural origins of the spatial heterogeneity remain unknown. On the other hand, extensive efforts have been devoted to understanding the atomic structure of metallic glasses. In particular, both icosahedronlike and crystal-like local structures have been experimentally observed in metallic glasses by electron diffraction [27–32]. In contrast, the direct correlation between these short-range order and nanoscale spatial heterogeneity has not been well explored. In this Letter, we investigate the local atomic structures corresponding to the spatial heterogeneity of a hyperquenched metallic glass by utilizing state-of-the-art spherical aberration corrected scanning transmission electron microscopy (STEM) and angstrom-beam electron diffraction (ABED), which provide a high spatial resolution for imaging in real space and for diffraction in reciprocal space, respectively.

A hyperquenched metallic glass $Zr_{53}Cu_{36}Al_{11}$ (at. %) with a nominal cooling rate of around 2.4×10^7 K s^{-1} is prepared by single-target rf magnetron sputtering at room temperature [12]. The experimental details for the TEM and ABED measurements are included in Supplemental Material [33]. The specimen used for ABED measurements is prepared by gentle ion milling with a thin edge of about 28 nm [34].

The amorphous nature of the hyperquenched metallic glass is verified by high-resolution TEM (HRTEM) and selected area electron diffraction (SAED). The homogeneous mazelike feature of the phase-contrast HRTEM micrograph as shown in Fig. 1(a), together with the homogeneous diffraction halo in the SAED pattern [inset in Fig. 1(a)], proves that the sample, prepared by gentle ion milling, is fully amorphous without any visible crystalline phase. However, when the sample is imaged by high-angle annual dark field scanning TEM (HAADF STEM), heterogeneous contrast with alternating dark and bright domains at the nanometer scale can be observed as shown in Figs. 1(b) and S1. The heterogeneous contrast in HAADF STEM images can also be viewed from the sample prepared by electrochemical polishing [Figs. 1(c) and S2]. Although the TEM samples are thinned by two different methods, the heterogeneous contrasts are very similar to each other. The hyperquenched metallic glass without any posttreatment is also characterized by AM AFM [35]. The phase shift mapping shows a nearly identical morphology and characteristic length of the spatial heterogeneity as those in the

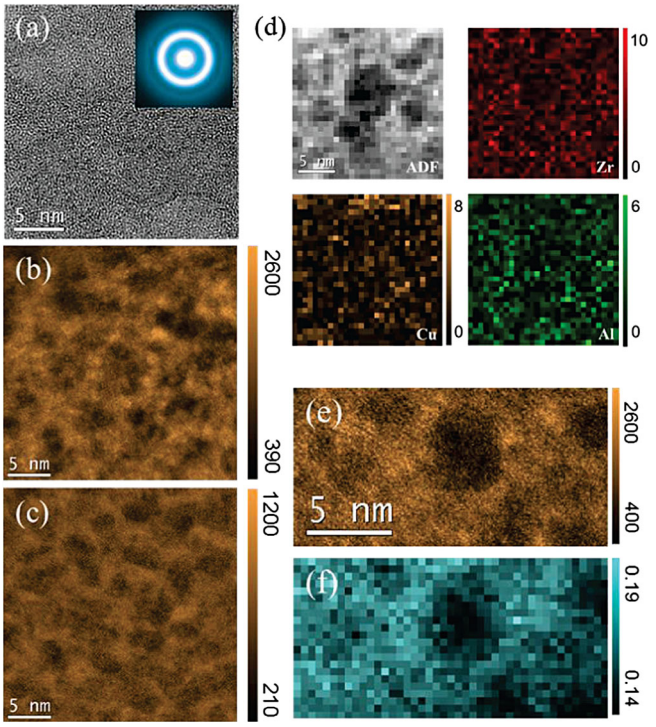

FIG. 1. Spatial heterogeneity of the hyperquenched metallic glass. (a) HRTEM observation of a sample prepared by ion milling. HAADF STEM images of samples prepared by (b) ion milling and (c) twin-jet polishing. (d) EDS mapping of the sample prepared by ion milling with a color scale showing the intensity of x-ray counts. (e) HAADF STEM image and (f) the corresponding map derived from the EELS zero-loss peak. The color scale for the EELS map indicates the values of the t/λ ratio, where t is the thickness of the sample and λ is the inelastic mean free path. The inset is the corresponding SAED pattern.

HAADF STEM images (see Fig. S3). The agreement between HAADF STEM and AM AFM images in the heterogeneous structure further confirms that the spatial heterogeneity imaged by HAADF STEM is an intrinsic feature of metallic glasses. We also inspected a melt-spun $Zr_{70}Cu_{29}Pt_1$ (at. %) metallic glass ribbon with an extremely thin edge for direct TEM characterization without any thinning. Again, a similar heterogeneous contrast can be observed in the milling-free sample by HAADF STEM (Fig. S4).

Since HAADF STEM is sensitive to the local chemistry and density, the heterogeneous contrast implies an inhomogeneous distribution of chemistry or density in metallic glasses. STEM energy-dispersive x-ray spectroscopy (EDS) mappings show that a visible chemical variation correlated with the heterogeneity cannot be detected in the sample down to the subnanoscale with quantitative measurements [see Fig. 1(d)]. The thickness map is derived from zero-loss peaks of EELS [Fig. 1(f)] according to the log-ratio technique [36]. As determined in Fig. S5, the contrast variation in the HAADF STEM images is mainly from the mass density difference between the dark and bright regions, which is evaluated to be approximately $9.2 \pm 1.5\%$ based on the HAADF and EELS zero-loss images [37]. The density variation between the dark and bright regions experimentally verifies the long-standing assumption on the coexistence of loosely and densely packed regions in metallic glasses [38]. Importantly, the length scale of the density variation is beyond short-range structural or chemical order.

The local atomic configurations in metallic glasses can be detected based on diffraction patterns from phase correlation among nearest-neighboring atoms by using ABED with a nearly parallel angstrom-sized electron beam [30,31]. Combining with the scanning function of STEM, a series of ABED patterns can be taken in a short period with a scan step of about 0.2 nm [Fig. 2(a)]. By selecting the ABED patterns solely from the bright or dark regions in HAADF STEM images, respectively, an integrated ABED pattern from either the bright or dark regions can be made by the superposition of the selected ABED patterns for statistical analyses on the structure of bright or dark regions [33]. The diffraction patterns in Figs. 2(b) and 2(c) are formed by integrating about 70 individual ABED patterns obtained from bright or dark regions, respectively. Apparently, the integrated ABED pattern taken from bright regions has a sharper and more uniform contrast than that

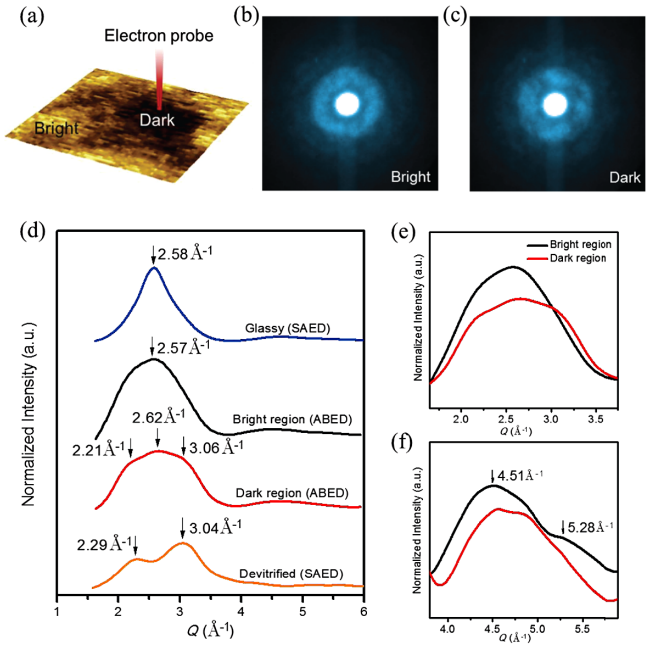

FIG. 2. Integrated ABED patterns from bright and dark regions. (a) A schematic illustration of scanning ABED measurements over spatially heterogeneous regions in the metallic glass. Integrated ABED patterns taken from (b) bright regions and (c) dark regions. (d) The intensity profiles derived from (b) and (c). For reference, the intensity profiles of SAED patterns taken from the hyperquenched metallic glass and the partially devitrified sample are also presented. Magnified views of the intensity profiles at (e) low Q and (f) high Q portions for bright and dark regions.

from dark regions. The intensity profiles in Fig. 2(d) are transferred from the two-dimensional integrated ABED patterns (see the method in Fig. S6). In Fig. 2(d), we can see that the normalized intensity profile taken from bright regions is very similar to that of the SAED pattern taken from the hyperquenched metallic glass over an area around 10 μm in diameter. However, two additional subpeaks at $Q \sim 2.21$ and 3.06 Å^{-1} can be observed in the intensity profile taken from dark regions. The feature of the two subpeaks is akin to that in the intensity profile of a SAED pattern of a partially devitrified sample annealed right below the crystallization onset temperature for 1 min [see Figs. 2(d) and S7], indicating that the dark regions may also contain a certain crystal-like order.

A direct comparison of the enlarged intensity profiles [Figs. 2(e) and 2(f)] reveals more structural differences between bright and dark regions. Although the two integrated ABED profiles contain the same number of individual ABED patterns, the intensity of the profile from the bright regions is much higher than that from the dark regions [see Fig. 2(e)], indicating stronger coherent scattering from the bright regions. The full width at half maximum of the profile from the bright regions (~1.2 Å^{-1}) is also obviously smaller than that from the dark regions (~1.4 Å^{-1}). Therefore, the bright regions appear more structurally ordered than the dark regions. Moreover, the intensity profile from the bright regions in Fig. 2(f) shows a peak shoulder around 5.28 Å^{-1} at the right side of the second peak, while we cannot see it from the profile of the dark regions. The Q ratios of the second peak and the shoulder to the first peak are calculated to be around 1.75 and 2.05, respectively. These two values are in accord with the theoretical values 1.71 and 2.04 for icosahedral order in metallic glasses [39,40]. Therefore, the integrated ABED analysis suggests that the bright regions in the HAADF STEM images contain well-defined icosahedral order while the dark regions contain detectable crystal-like order.

The local atomic structures of bright and dark regions can be obtained by analyzing the diffraction vectors of individual ABED patterns taken from these regions. Since individual ABED patterns are from a very small volume of the sample, they may or may not represent the typical structural features of the glass. To solve this issue, we selected the ABED patterns which directly contribute to the peaks of the intensity profiles in Fig. 2(d). The consistence between the individual ABED pattern and the statistical profile can ensure that the selected ABED patterns represent the most common structural features of bright or dark regions. Figure 3(a) shows one representative ABED pattern taken from bright regions in the HAADF STEM image. The dashed ring which passes through most diffraction spots at $Q \sim 2.57$ Å^{-1} is in accord with the major peak at $Q \sim 2.57$ Å^{-1} in the intensity profile of bright regions [Fig. 2(d)] and the SAED pattern of metallic glass taken from a large area [Fig. 3(c)]. The angles between diffraction vectors marked in Fig. 3(b) are close to those of a distorted icosahedron along a fivefold orientation [31]. The ABED pattern corresponding to the fcc-like order from a distorted icosahedron can also be observed in the bright regions (Fig. S8). The ABED patterns further confirm that the atomic structure in the bright regions has a noticeable icosahedral order. In comparison with those from the bright regions, the ABED patterns taken from dark regions usually have weak and broad diffraction spots as shown in Figs. 3(d) and S9, indicating relatively more structural disorder in the regions. However, as a common feature, the diffraction spots in the ABED patterns from dark regions can be marked by two dashed rings located at $Q \sim 2.21$ and 3.06 Å^{-1}, which are in accord with the peaks in the intensity profiles of integrated ABED [Fig. 2(d)] and the SAED pattern obtained from a partially devitrified sample [Fig. 3(f)] that has a tetragonal crystal-like order. Moreover, the sum of two adjacent angles between diffraction vectors is close to 90° [Fig. 3(e)], further confirming the formation of the tetragonal-related order in the low-density dark regions [Fig. S10]. The ABED patterns corresponding to tetragonal-related order can be often observed in the dark regions. Figure 4 shows two more examples in which the major diffraction

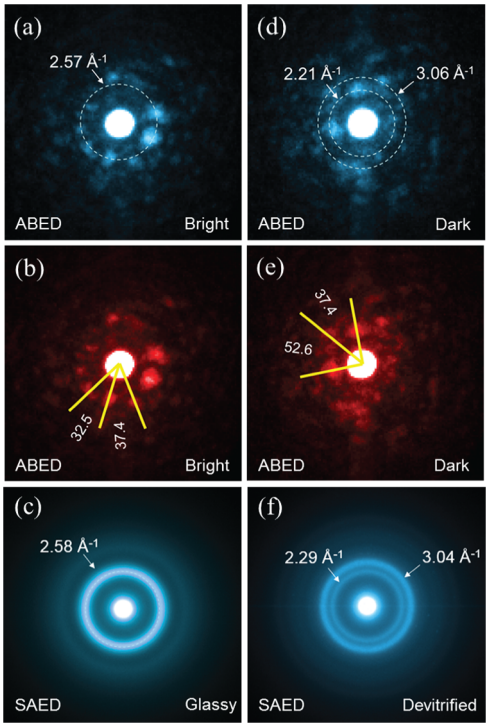

FIG. 3. Representative ABED patterns for bright and dark regions. Individual ABED patterns taken from (a) bright regions and (d) dark regions. The dashed white rings correspond to the peak positions of the intensity profiles of the integrated ABED. The angles between diffraction vectors are marked in (b) and (e). SAED patterns taken from (c) the as-prepared hyperquenched metallic glass and (f) the partially devitrified metallic glass.

spots locate at the cycles of $Q \sim 2.62$ Å^{-1}, one of the characteristic peaks in the integrated ABED profile of dark regions [Fig. 2(d)]. In Fig. 4(b), the angles between diffraction vectors are around 45°, and the sum of two adjacent angles is close to 90°, while for the ABED pattern shown in Fig. 4(f), the diffraction vectors have an angle of about 60°. The two ABED patterns can be marked as the diffraction from a stretched body-centered cubic (bcc)-like structure (similar to a distorted rectangular prism) along the [100] and [111] directions, respectively. However, it is worth noting that crystal-like lattice fringes cannot be found by high-resolution TEM and STEM, although the tetragonal crystal-like order can be detected in reciprocal space by ABED. This indicates that the crystal-like order may exist only in a very short range together with severe geometric frustration [31].

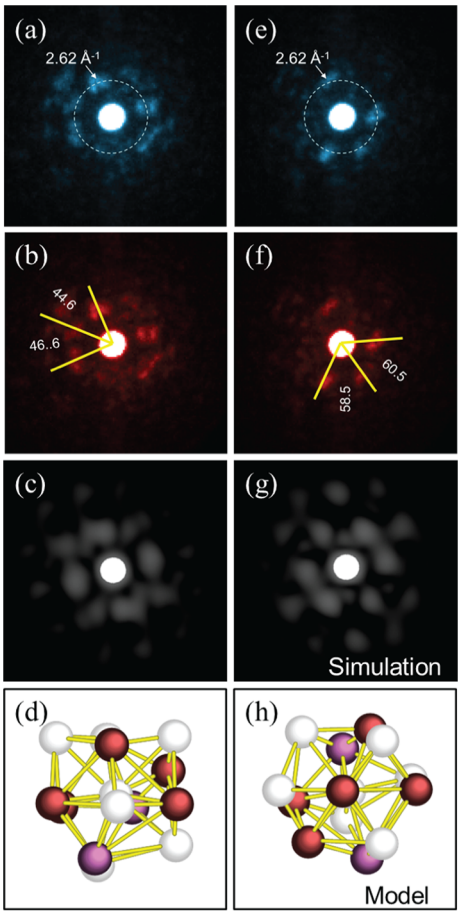

FIG. 4. ABED patterns showing tetragonal crystal-like order in dark regions. Experimental ABED patterns (a) and (d) are taken from a stretched bcc (or distorted rectangular prism) structure along the [100] and [111] directions in dark regions, respectively. The dashed white rings are located at the corresponding peak position of the intensity profile of the integrated ABED. The angles between diffraction vectors are marked in (b) and (f). For comparison, simulated ABED patterns (c) and (g) are calculated from an atomic configuration with a stretched bcc structure along the (d) [100] and (h) [111] directions, respectively. The atomic configuration is a Zr-centered atomic cluster with a Voronoi index of $\langle 0\,4\,4\,5 \rangle$ taken from the MD model where Zr atoms are marked as white spheres, Cu atoms brown spheres, and Al purple spheres.

The combination of HAADF STEM and ABED demonstrates that the spatial heterogeneity of metallic glasses has a close correlation with structural variations, which results in a density fluctuation, while an obvious chemical composition fluctuation cannot be seen. The bright regions in the HAADF STEM have a relatively high density and more icosahedral order. In contrast, the dark regions have a lower density and lower structure ordering but contain a certain crystal-like tetragonal order. Based on the effective packing theory [41] and MD simulations [42,43] (see details in Fig. S11) of a hyperquenched Zr-Cu-Al metallic glass, the icosahedral order is usually from Cu- or Al-centered clusters with a relatively dense packing, while the crystal-like order is associated with Zr-centered clusters with a large number of coordinated atoms from 13 to 17. Although crystal-like order is expected to give rise to an effective atomic packing because of high symmetry, the Zr-centered clusters actually have relatively loose atomic arrangements caused by a large difference in the bonding lengths among Zr-Zr (3.16 Å), Zr-Cu (2.85 Å), and Zr-Al (3.01 Å) and thus significant geometric frustration. The local structure scenario revealed by ABED certainly coincides with our previous synchrotron XRD and EXAFS characterizations of hyperquenched Zr-based metallic glasses [44]. The dark regions with lower density and higher disorder appear to be dominated by Zr-center clusters with longer interatomic bonds and more significant geometric frustration, while the dense bright regions are mainly occupied by well-developed Cu- and Al-center icosahedronlike clusters.

The two distinct structural assemblies in spatial heterogeneity can account for many important phenomena of metallic glasses. By combining differential scanning calorimetry and AM AFM, the dark regions have been found to shrink with the release of excess enthalpy [12], which act as fertile sites for the localized translational motions of atoms during β relaxation [45]. Moreover, due to the relatively loose packing and the size analogue with STZs [17–20], dark regions might also contribute to the nonlinear deformation of metallic glasses [6,7,46]. Interestingly, it has recently been found that the metallic glass-forming ability is strongly correlated with the stability of crystal-like order under annealing below the glass transition temperature T_g [47], indicating that the glass-forming ability has a certain relation with the spatial heterogeneity. The icosahedral order in bright regions might correlate with the slow dynamics and the stability of supercooled liquids [48–51] of metallic glasses. The coexistence of icosahedral order and crystal-like order in the metallic glass may provide new insights into the fractal nature of medium-range order [52,53] and elastic moduli inheritance of solvent atoms [54] in metallic glasses.

In summary, the local atomic order corresponding to spatial heterogeneity in a hyperquenched metallic glass has

been systematically studied by Cs-corrected STEM and ABED. A local structure characterization demonstrates that the spatial heterogeneity has a direct correlation with local atomic configuration variation, which gives rise to a density fluctuation and thus nanosized bright and dark domains in HAADF STEM images. The densely packed bright regions have well-defined icosahedronlike order, while the loosely packed dark regions are more disordered with a certain tetragonal crystal-like order. Our study clarifies the inherent relationship between the local atomic order and the spatial heterogeneity in metallic glasses and provides experimental insight into the nature of structural inhomogeneity of metallic glasses.

This work was sponsored by MOST 973 of China (Grant No. 2015CB856800), National Natural Science Foundation of China (Grants No. 11327902, No. 51271113, and No. 11704245). F. Z. is supported by the International Postdoctoral Exchange Fellowship Program of China. We thank the support of JASRI/SPring-8 under Proposals No. 2013A1539 and No. 2013B1197 and the SR16000 supercomputing facilities from Center for Computational Materials Science of the Institute for Materials Research, Tohoku University.

F. Z. and A. H. contributed equally to this work.

*Corresponding author.
mwchen@jhu.edu

[1] A. S. Argon and H. Y. Kuo, Mater. Sci. Eng. **39**, 101 (1979).
[2] T. C. Hufnagel, C. A. Schuh, and M. L. Falk, Acta Mater. **109**, 375 (2016).
[3] E. Ma, Nat. Mater. **14**, 547 (2015).
[4] M. W. Chen, Annu. Rev. Mater. Res. **38**, 445 (2008).
[5] W. H. Wang, Y. Yang, T. G. Nieh, and C. T. Liu, Intermetallics **67**, 81 (2015).
[6] W. Dmowski, T. Iwashita, C. P. Chuang, J. Almer, and T. Egami, Phys. Rev. Lett. **105**, 205502 (2010).
[7] J. C. Ye, J. Lu, C. T. Liu, Q. Wang, and Y. Yang, Nat. Mater. **9**, 619 (2010).
[8] Z. Wang, B. A. Sun, H. Y. Bai, and W. H. Wang, Nat. Commun. **5**, 5823 (2014).
[9] J. Ding, Y. Q. Cheng, H. W. Sheng, M. Asta, R. O. Ritchie, and E. Ma, Nat. Commun. **7**, 13733 (2016).
[10] S. V. Ketov, Y. H. Sun, S. Nachum, Z. Lu, A. Checchi, A. R. Beraldin, H. Y. Bai, W. H. Wang, D. V. Louzguine-Luzgin, and A. L. Greer, Nature (London) **524**, 200 (2015).
[11] H. B. Yu, X. Shen, Z. Wang, L. Gu, W. H. Wang, and H. Y. Bai, Phys. Rev. Lett. **108**, 015504 (2012).
[12] F. Zhu, H. K. Nguyen, S. X. Song, D. P. B. Aji, A. Hirata, H. Wang, K. Nakajima, and M. W. Chen, Nat. Commun. **7**, 11516 (2016).
[13] P. Luo, Y. Z. Li, H. Y. Bai, P. Wen, and W. H. Wang, Phys. Rev. Lett. **116**, 175901 (2016).
[14] Q. Wang, S. T. Zhang, Y. Yang, Y. D. Dong, C. T. Liu, and J. Lu, Nat. Commun. **6**, 7876 (2015).
[15] M. D. Ediger, Annu. Rev. Phys. Chem. **51**, 99 (2000).
[16] F. Spaepen, Acta Metall. **25**, 407 (1977).
[17] A. S. Argon, Acta Metall. **27**, 47 (1979).
[18] M. L. Falk and J. S. Langer, Phys. Rev. E **57**, 7192 (1998).
[19] W. L. Johnson and K. Samwer, Phys. Rev. Lett. **95**, 195501 (2005).
[20] D. Pan, A. Inoue, T. Sakurai, and M. W. Chen, Proc. Natl. Acad. Sci. U.S.A. **105**, 14769 (2008).
[21] Y. Fan, T. Iwashita, and T. Egami, Nat. Commun. **5**, 5083 (2014).
[22] Y. Fan, T. Iwashita, and T. Egami, Phys. Rev. Lett. **115**, 045501 (2015).
[23] H. Wagner, D. Bedorf, S. Küchemann, M. Schwabe, B. Zhang, W. Arnold, and K. Samwer, Nat. Mater. **10**, 439 (2011).
[24] Y. H. Liu, D. Wang, K. Nakajima, W. Zhang, A. Hirata, T. Nishi, A. Inoue, and M. W. Chen, Phys. Rev. Lett. **106**, 125504 (2011).
[25] Y. Yang, J. F. Zeng, A. Volland, J. J. Blandin, S. Gravier, and C. T. Liu, Acta Mater. **60**, 5260 (2012).
[26] L. S. Huo, J. F. Zeng, W. H. Wang, C. T. Liu, and Y. Yang, Acta Mater. **61**, 4329 (2013).
[27] W. G. Stratton, J. Hamann, J. H. Perepezko, P. M. Voyles, X. Mao, and S. V. Khare, Appl. Phys. Lett. **86**, 141910 (2005).
[28] J. Saida, M. Matsushita, and A. Inoue, Appl. Phys. Lett. **79**, 412 (2001).
[29] J. Hwang, Z. H. Melgarejo, Y. E. Kalay, I. Kalay, M. J. Kramer, D. S. Stone, and P. M. Voyles, Phys. Rev. Lett. **108**, 195505 (2012).
[30] A. Hirata, P. F. Guan, T. Fujita, Y. Hirotsu, A. Inoue, A. R. Yavari, T. Sakurai, and M. W. Chen, Nat. Mater. **10**, 28 (2011).
[31] A. Hirata, L. J. Kang, T. Fujita, B. Klumov, K. Matsue, M. Kotani, A. R. Yavari, and M. W. Chen, Science **341**, 376 (2013).
[32] A. C. Y. Liu, M. J. Neish, G. Stokol, G. A. Buckley, L. A. Smillie, M. D. de Jonge, R. T. Ott, M. J. Kramer, and L. Bourgeois, Phys. Rev. Lett. **110**, 205505 (2013).
[33] See Supplemental Material at http://link.aps.org/supplemental/10.1103/PhysRevLett.119.215501 for experimental details and Figs. S1–S11.
[34] D. T. Schweiss, J. Hwang, and P. M. Voyles, Ultramicroscopy **124**, 6 (2013).
[35] R. Garcia, C. J. Gomez, N. F. Martinez, S. Patil, C. Dietz, and R. Magerle, Phys. Rev. Lett. **97**, 016103 (2006).
[36] T. Malis, S. C. Cheng, and R. F. Egerton, J. Electron Microsc. Tech. **8**, 193 (1988).
[37] V. Schmidt, H. Rösner, M. Peterlechner, G. Wilde, and P. M. Voyles, Phys. Rev. Lett. **115**, 035501 (2015).
[38] T. Egami, K. Maeda, and V. Vitek, Philos. Mag. A **41**, 883 (1980).
[39] S. Sachdev and D. R. Nelson, Phys. Rev. Lett. **53**, 1947 (1984).
[40] K. F. Kelton, G. W. Lee, A. K. Gangopadhyay, R. W. Hyers, T. J. Rathz, J. R. Rogers, M. B. Robinson, and D. S. Robinson, Phys. Rev. Lett. **90**, 195504 (2003).
[41] T. Egami and Y. Waseda, J. Non-Cryst. Solids **64**, 113 (1984).
[42] S. Plimpton, J. Comput. Phys. **117**, 1 (1995).

[43] T. Fujita, K. Ohara, K. Miura, A. Hirata, M. Kotani, Y. Nishiura, and M. W. Chen, Europhys. Lett. **110**, 38002 (2015).
[44] Y. H. Liu, T. Fujita, D. P. B. Aji, M. Matsuura, and M. W. Chen, Nat. Commun. **5**, 3238 (2014).
[45] J. C. Qiao, Y. J. Wang, J. M. Pelletier, L. M. Keer, M. E. Fine, and Y. Yao, Acta Mater. **98**, 43 (2015).
[46] Y. C. Wu, B. Wang, Y. C. Hu, Z. Lu, Y. Z. Li, B. S. Shang, W. H. Wang, H. Y. Bai, and P. F. Guan, Scr. Mater. **134**, 75 (2017).
[47] P. Zhang, J. J. Maldonis, M. F. Besser, M. J. Kramer, and P. M. Voyles, Acta Mater. **109**, 103 (2016).
[48] H. Shintani and H. Tanaka, Nat. Phys. **2**, 200 (2006).
[49] F. C. Frank, Proc. R. Soc. A **215**, 43 (1952).
[50] J. Li, Y. Cao, C. Xia, B. Kou, X. Xiao, K. Fezzaa, and Y. J. Wang, Nat. Commun. **5**, 5014 (2014).
[51] Y. C. Hu, F. X. Li, M. Z. Li, H. Y. Bai, and W. H. Wang, Nat. Commun. **6**, 8310 (2015).
[52] D. Z. Chen, C. Y. Shi, Q. An, Q. Zeng, W. L. Mao, W. A. Goddard, and J. R. Greer, Science **349**, 1306 (2015).
[53] D. Ma, A. D. Stoica, and X. L. Wang, Nat. Mater. **8**, 30 (2009).
[54] D. Ma, A. D. Stoica, X. L. Wang, Z. P. Lu, B. Clausen, and D. W. Brown, Phys. Rev. Lett. **108**, 085501 (2012).